JOURNAL OF MATERIALS SCIENCE: MATERIALS IN MEDICINE **10** (1999) 135–145

Characterization of porous hydroxyapatite

K. A. HING, S. M. BEST, W. BONFIELD
IRC in Biomedical Materials, Queen Mary and Westfield College, Mile End Road, London, E1 4NS, UK

Hydroxyapatite has been considered for use in the repair of osseous defects for the last 20 years. Recent developments have led to interest in the potential of porous hydroxyapatite as a synthetic bone graft. However, despite considerable activity in this field, regarding assessment of the biological response to such materials, the basic materials characterization is often inadequate. This paper documents the characterization of the chemical composition, mechanical integrity, macro- and microstructure of a porous hydroxyapatite, Endobon® (E. Merck GmbH), intended for the bone-graft market. Specimens possesed a range of apparent densities from 0.35 to 1.44 g cm^{-3}. Chemical analysis demonstrated that the natural apatite precursor of Endobon® was not converted to pure hydroxyapatite, but retained many of the ionic substituents found in bone mineral, notably carbonate, sodium and magnesium ions. Investigation of the microstructure illustrated that the struts of the material were not fully dense, but had retained some traces of the network of osteocyte lacunae. Macrostructural analysis demonstrated the complex inter-relationship between the structural features of an open pore structure. Both pore size and connectivity were found to be inversely dependent on apparent density. Furthermore, measurement of pore aspect ratio and orientation demonstrated a relationship between apparent density and the degree of macrostructural anisotropy within the specimens, while, it was also noted that pore connectivity was sensitive to anisotropy. Compression testing demonstrated the effect of apparent density and macrostructural anisotropy on the mechanical properties. An increase in apparent density from 0.38 to 1.25 g cm^{-3} resulted in increases in ultimate compressive stress and compressive modulus of 1 to 11 MPa and 0.2 to 3.1 GPa, respectively. Furthermore, anisotropic high density (> 0.9 g cm^{-3}) specimens were found to possess lower compressive moduli than isotropic specimens with equivalent apparent densities. These results underline the importance of full structural and mechanical characterization of porous ceramic implant materials.

1. Introduction

As surgical technique and medical knowledge continue to advance, there is an increasing demand for synthetic bone replacement materials, resulting from the limited supply of autograft material and the health risks associated with the use of allografts. Hydroxyapatite has been investigated for use in the osseous environment for over 20 years [1–4] and the biocompatibility of the ceramic and its osseoconductive behavior is well established [4–7]. Consequently, there is increasing interest in the development of synthetic porous hydroxyapatite (HA) bone replacement materials for the filling of both load-bearing and non-load-bearing osseous defects, with the potential for restoration of vascularity and complete penetration of osseous tissue throughout the repair site. However, while considerable work has been performed to investigate the *in vivo* and *in vitro* response of dense and porous hydroxyapatite [4–13], generally the materials characterization of these materials is inadequate.

The morphology of ceramic implants has been considered since the use of porous materials were first described in 1963 [14] and in 1972 Hulbert *et al.* [15] demonstrated that porous discs of a near inert ceramic exhibited thinner fiberous encapsulation with faster healing in surrounding muscle and connective tissue when compared with dense discs of the same composition implanted in the same site. It was postulated that this resulted from mechanical interlock, which reduced motion between host tissue and implant, eliciting a more passive response from the host. A minimum pore size of approximately 100–150 μm has been established as necessary for the continued health of bony ingrowth [16]; however, a number of groups have suggested that the degree of interconnectivity is more critical than the pore size [10–12], although, few techniques for assessment of connectivity from plane sections are reported. Image analysis has been studied as a technique for the quantification of macrostructure by a number of groups, [17–19]. Generally, methods which were based on the use of simple, computer defined, measurement parameters, such as feature area and dimensions, were most successful due to increased reproducibility, resulting from a reduction in operator dependence.

Knowledge of the chemical content of any implant is important from a perspective of possible toxin contamination. However, interest has recently developed in the substitution of controlled levels of different elements into the hydroxyapatite lattice to enhance biocompatibility [20, 21]. *In vivo*, bone mineral is produced in the presence of many complex and varied physiological fluids resulting in the formation of a highly imperfect apatite, with significant carbonate substitution for PO_4^{3-} and trace levels of a number of ions substituting for Ca^{2+} and OH^- [22, 23]. This is in contrast to synthetic HA which tends to lose any associated carbonate ions unless sintered under controlled atmospheric conditions [24–27]. These substituents play an important role in the mineral homeostasis and metabolic processes of the surrounding cells and tissue [28, 29]. Hence, the presence of controlled levels of the appropriate ionic species in any synthetic hydroxyapatite could be biologically advantageous, although care must be exercised when considering the merits of ionic substituents. Micromolar concentrations of aluminum and silicon ions have been reported to stimulate osteoblast proliferation and differentiation [20]; however, high concentrations of aluminum have been demonstrated to suppress bone mineral formation [28]. The degree of crystallinity and the phase purity of the apatite present are also important parameters to characterize. Variations in the precise nature of the calcium phosphate phases present have been demonstrated to have a strong effect on cellular response [8, 9, 11, 13]. Furthermore, changes in the degree of crystallinity and phase purity also lead to variations in the level of specimen solubility [10–12, 30].

Conventional methods of mechanical characterization such as tensile, biaxial and impact testing are unsuitable when applied to porous materials due to the difficulties encountered in machining and gripping test pieces without causing pre-damage [31]. Compression testing has been successfully used by a number of authors in the characterization of cancellous bone and has also been adopted in the testing of porous and dense hydroxyapatite [12, 19]. However, in addition to difficulties resulting from the inherent variation in porous samples, testing conditions must be carefully controlled. Comprehensive investigations [32, 33] into a number of key test-piece parameters, such as specimen shape, aspect ratio and size, have demonstrated that cylindrical specimens with an aspect ratio of 2 : 1 (length:diameter) should be standardized for compression testing of high porosity materials.

The mechanical properties of highly porous ceramics (90–60% porosity) have been successfully predicted in [34, 35] by modeling the structure as an elastic–brittle foam. The relationships derived between ultimate compressive stress, σ_c, compressive modulus, E_c, and apparent density, ρ, were of the form

$$\sigma_c \propto c_a \rho^x \quad (1)$$

$$E_c \propto c_b \rho^y \quad (2)$$

Where, for isotropic foams, $x = 2$ and $y = 2$ or 3 depending on whether the structure was open or closed, respectively. However, for anisotropic foams the direction of testing was found to influence the dependency. If tested in the transverse direction (perpendicular to the longest pore dimension), then $x = 2$ and $y = 1$ or 3, while if tested in the longitudinal direction (parallel to the longest pore dimension) then $x = 1$ and $y = 1$, irrespective of the degree of structural connectivity. This work highlights the level of sensitivity that the mechanical properties have to both the apparent density and the structural texture or isotropy of a porous ceramic. Hence, for accurate understanding and prediction of the mechanical behavior of a porous material, full physical characterization (i.e. determination of both apparent density and analysis of the porous texture) of the porous macrostructure should be performed.

This paper details the chemical, structural and mechanical examination of a commercially available porous hydroxyapatite, Endobon®, whose main feature is the preservation of the open macroporous structure of bovine cancellous bone. Initial findings concerning the biological response to the material have been previously reported [36] while the effect of the porous structure on the biological response will be reported in future publications.

2. Materials and methods

2.1. Materials

The material used in this study is a commercially available porous hydroxyapatite, Endobon®, produced by Merck GmbH (Darmstadt, Germany). The material is manufactured from natural cancellous bone, via a technique which allows the removal of the organic component of cancellous bone, while preserving the trabecular structure, and hydrothermally converting the bone mineral and amorphous inorganic components within cancellous bone into hydroxyapatite. The final product is a porous hydroxyapatite with a three-dimensional interconnecting network of pores. Specimens were cylindrical in geometry with a length of 8.76 ± 0.40 mm and a diameter of 4.58 ± 0.06 mm, equating to an aspect ratio of approximately 2 : 1 (length : diameter). Chemical and mechanical characterization was performed on 50 specimens selected to provide a range of isotropic and anisotropic samples, with apparent densities of between 0.35–1.44 g cm^{-3} (Fig. 1a). Specimens for structural characterization were segregated according to their apparent density, to create three distinct batches of specimens with mean apparent densities of 0.62 ± 0.03 (Batch B), 0.92 ± 0.03 (Batch C) and 1.18 ± 0.06 (Batch A) g cm^{-3} (Fig. 1b).

2.2. Chemical analysis

Endobon® specimens were carefully ground into a fine powder using a pestle and mortar and analyzed using X-ray fluorescence (XRF) (Ceram Research, Stoke-on-Trent, UK). Phase purity was assessed using X-ray diffractometry (XRD), performed on a Siemens D-5000 X-ray diffractometer in flat plate geometry with CuK_α radiation. Data were acquired from 5–110° 2θ, with a step size of 0.02° at 12 s per step. Infrared spectroscopy was performed using a Nicolet 800 System Fourier transform infrared (FT-IR) spectrometer, fitted with a

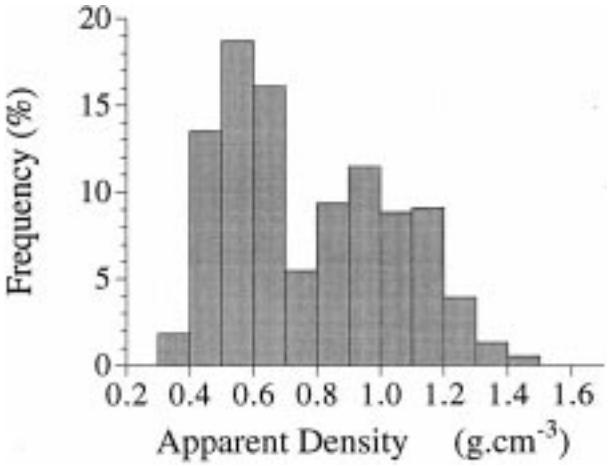

(a)

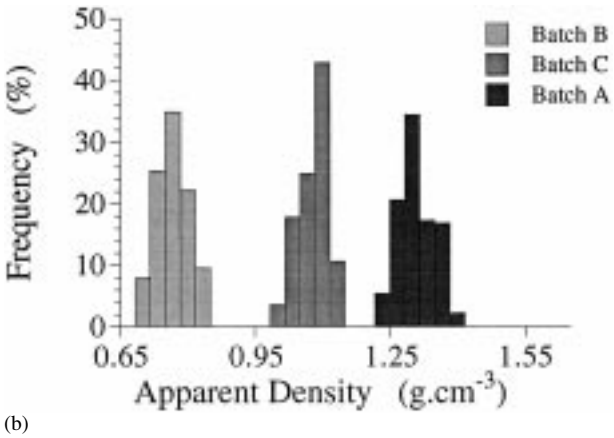

(b)

Figure 1 Density distributions of (a) all specimens and (b) specimens in Batches B, C and A.

photo-acoustic sampler, at a resolution of four wave numbers, operating from 4000 to 400 cm^{-1}.

2.3. Physical characterization

The physical characterization was split into three structural levels; measurement of bulk specimen density, characterization of macrostructure and characterization of microstructure.

2.3.1. Specimen density

Both apparent and real densities were calculated for each specimen, where apparent density includes the open and closed porosity in the volume of a structure and real density includes only the closed porosity in the volume of a structure. Apparent density was calculated from the dry weight and volume of each specimen using Equation 3. The real density of Endobon® specimens was determined using Equation 4. For the measurement of submerged weight a vacuum embedding device (Struers, UK) was used to ensure penetration of water into all internal, open porosity. The percentage of closed porosity present in the HA struts, was calculated as in Equation 5.

$$\text{Apparent density} = \frac{W_{\text{dry}}}{\pi(r^2)1} \quad (3)$$

$$\text{Real density} = \left(\frac{W_{\text{dry}}}{W_{\text{dry}} - W_{\text{sub}}}\right) \times \rho H_2O \quad (4)$$

$$\text{Closed porosity} = \left(1 - \frac{\text{real density}}{\rho HA}\right) \quad (5)$$

Where W_{dry} is the dry weight, r is the specimen radius, 1 is the specimen length, W_{sub} is the weight when submerged in deionized water, ρH_2O is the density of water at measurement temperature, and ρHA is the theoretical density of HA (assumed to be 3.156 g. cm^{-3}).

2.3.2. Microscopy and image analysis

Specimens selected for micro- and macroporosity investigations were vacuum embedded in epoxy resin and serial-sectioned longitudinally (three sections per specimen). These sections were then re-embedded and polished to a 1 μm surface finish. Sections were etched with a 2.5% aqueous solution of phosphoric acid to reveal the grain structure. Scanning electron microscopy (SEM) was performed using a Jeol 6300 series SEM. Light microscopy was performed using a Zeiss Axioskop microscope, employing both dark and bright field reflected illumination. Micrographs taken at magnifications of × 25, × 1000 and × 2000 were used for analysis of macrostructure, microporosity and grain size, respectively. Image analysis was performed on Quantimet 570 equipment and images were acquired through a charge-coupled device (CCD) camera linked either directly to the light microscope or, where scanning electron micrographs were studied, mounted with a 35–70 mm zoom lens, at 50 mm with an aperture setting of 2.8. Endobon® specimens analyzed for macrostructure were aligned with the long axis of the cylindrical specimen running horizontally across the video image. After detection of either the macro- or microfeatures, parameters such as feature area, length, breadth and pore orientation were measured.

2.3.3. Grainsize, pore morphology and connectivity

Equivalent circular diameters of the individual grains (G_d) and pores (P_d) were calculated from the measured feature areas (Equation 6)

$$G_d \text{ or } P_d = \left(\frac{\text{Feature Area}}{\pi}\right)^{\frac{1}{2}} \times 2 \quad (6)$$

However, although acceptable for equiaxed grains and micropores, this method was not appropriate for the predominately elliptical or elongated macropores. Therefore, pore lengths (P_1) and breadths (P_b) were also measured, where the pore length is the dimension of the longest axis, and pore breadth the longest dimension perpendicular to the length. Macropore shape was assessed by calculating the aspect ratio from P_1 and P_b. Macropore orientation, the angle of deviation from the horizontal of the longest axis of a pore, was measured in the assessment of anisotropy. Connectivity of the macroporosity within the structure was assessed by

measurement of the number of whole macropores identified within the measurement frame area (Equation 7). Frame areas of 9 and 16 mm^2 were used, and, within this study, frame area was not found to influence the results. This approach was selected because interpretation of the usual features measured in the assessment of connectivity, such as pore interconnections (pore junctions), or measurement of the ratio of isolated and interconnected pores, was found not to be feasible over the entire range of densities assessed. This resulted from the difficulty in determining whether a detected feature was an irregularly shaped pore or a number of interconnected pores wherever the interconnection diameter approached that of the pores. Hence, measurement of the distinct number of pore junctions or interconnected pores was impractical in anisotropic and low to medium density material. However, where measurement of the number of pore junctions was feasible, calculation of the number of pore junctions per pore was a good measure of pore connectivity.

$$\text{Connectivity indicator} = \left(\frac{\text{Frame area}}{\text{Number of pores}}\right) \quad (7)$$

2.4. Mechanical testing

Compression testing was performed using an Instron 4464 bench-top test machine fitted with a 2 kN load cell. Testing was performed under computer control and load was applied axially to the specimens with a crosshead velocity of 0.1 mm min^{-1}, until catastrophic brittle failure occurred.

3. Results

3.1. Chemical analysis

The Ca : P ratio and the principal elements detected by XRF are outlined in Table I. The Ca:P ratio was found to be in excess of the theoretical value of 1.67, indicating either the presence of up to 1 wt % CaO phase impurity, or phosphate deficiency in the powder specimens. The XRF results also revealed that Endobon® contained significant and consistent levels of magnesium and sodium in comparison with synthetic materials, which typically contain 0.27 and < 0.03 oxide wt %, respectively [9]. Low (< 0.1 oxide wt %) levels of strontium, zinc and barium were detected. Significant quantities of aluminum and silicon were detected in only one sample, otherwise there was little chemical variation between powder samples.

Good agreement was found between the XRD patterns obtained from Endobon® powder (Fig. 2a) and the International Committee for Diffraction Data (ICDD) powder diffraction file for hydroxyapatite [37], however a small peak at 37.4° was also present, indicating the presence of 1–2 wt % CaO [38]. The FT-IR spectra obtained from the Endobon® powder (Fig. 2b) exhibited a range of peaks from 1400–1550 cm^{-1} in addition to the peaks expected for hydroxyapatite (i.e. those related to the PO_4^{3-} and OH^- groups). These peaks corresponded to the CO_2^{3-} ν3 vibration modes associated with CO_2^{3-} groups involved in both Type A and B carbonate substitution. Despite drying the power at 80 °C for over 24 h there was also a broad peak around 3000 cm^{-1} demonstrating the presence of adsorbed water.

TABLE I Results of XRF (figures quoted are oxide weight percentage of total ash)

(wt %)	CaO	P_2O_5	Ca:P	MgO	Na_2O	SrO	ZnO	BaO	Al_2O_3	SiO_2
EP1	55.6	41.8	1.68	1.00	0.67	0.03	0.03	0.02	<0.02	<0.02
EP2	55.4	41.8	1.67	0.86	0.68	0.03	0.02	0.02	<0.02	<0.02
EP3	55.2	41.7	1.68	1.06	0.76	0.08	0.02	0.02	<0.02	<0.02
EP4	55.3	41.6	1.68	0.80	0.55	0.06	0.02	0.02	0.12	0.03
Mean	55.4	41.7	1.68	0.93	0.67	0.05	0.02	0.02	–	–
SD	0.2	0.1	0.01	0.12	0.09	0.02	0.01	–	–	–

3.2. Physical characterization

3.2.1. Specimen density

Apparent density was found to range from 0.35 to 1.44 g cm^{-3} within the population of 350 specimens. However, the real density did not demonstrate the same degree of variation with a mean value of 3.039 ± 0.005 g cm^{-3}, which equates to a closed microporosity of $3.7 \pm 0.3\%$.

3.2.2. Macrostructure

Optical microscopy demonstrated that the specimens possessed highly interconnected (open) porosity, however, it was clear that the degree of pore connectivity was dependent on both the apparent density (Fig. 3a) and the

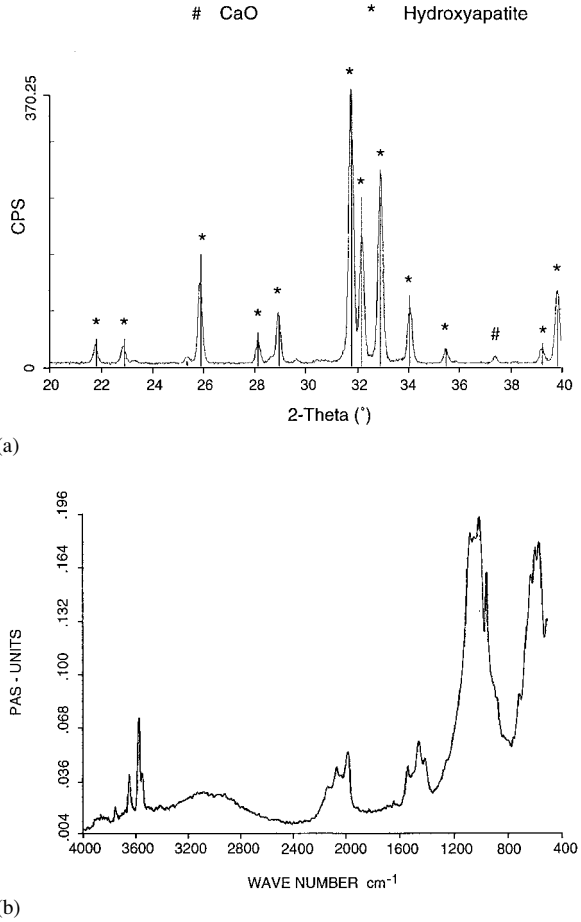

Figure 2 (a) XRD pattern for Endobon®, demonstrating the presence of CaO. (b) FT-IR spectrum for Endobon®.

degree of isotropy (Fig. 3b) of the specimen. This duel dependency prohibited the accurate identification of individual structural relationships, however, there are some trends evident in the variation of macropore size and morphology, with apparent density. As expected, the mean and modal macropore sizes were found to increase with decreasing apparent density (Table II). However, batch B specimens were found to possess wider size distributions than the other batches (Fig. 4a) reflecting a lack of uniformity in the macrostructure at lower densities. Similarly, batch B macropores possessed larger aspect ratios (Fig. 5a), indicating a tendency to non-spherical shaped pores in these specimens. Moreover, correlation between macropore aspect ratio and orientation in batch B specimens (Fig. 5b) demonstrated that these specimens were predominately anisotropic and that anisotropy was exhibited as an alignment of the long axis of high aspect ratio pores with the long axis of the cylindrical specimen. Connectivity was found to be influenced by both macrostructural anisotropy and apparent density, with the influence of apparent density on connectivity being stronger for isotropic specimens, particularly for specimens with higher apparent densities (Fig. 6).

3.2.3. Microstructure

Both micropore and grain size were found to be independent of specimen apparent density. SEM demonstrated that microporosity could be classified into two groups, divisible by size. Micropores $< 3\,\mu m$ in size tended to be isolated spherical pores, which were randomly distributed throughout the ceramic struts, located at grain boundaries, triple points and occasion-

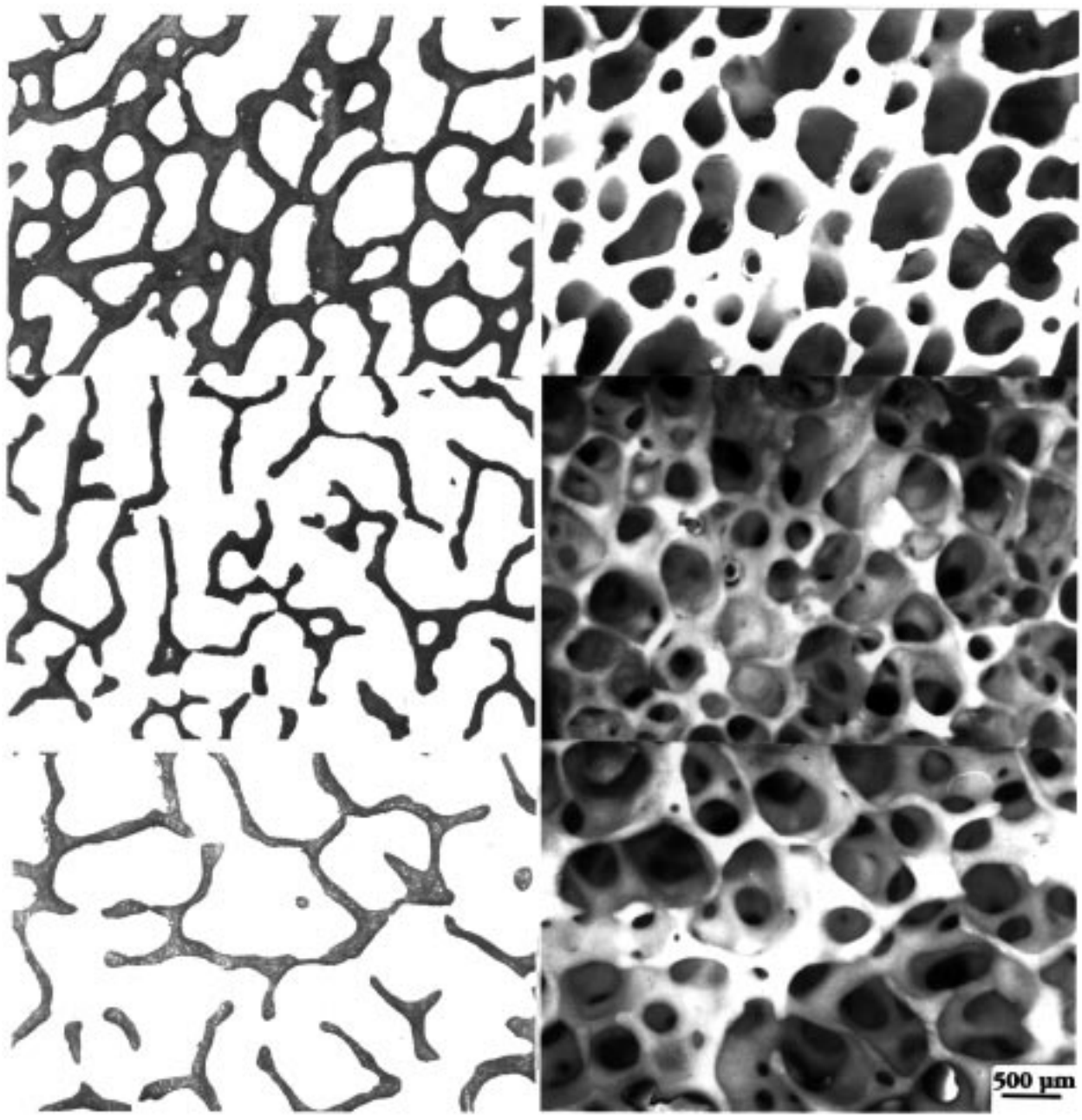

(a)

Figure 3 (a) Optical micrographs demonstrating the effects of density variation on macrostructure in isotropic specimens.

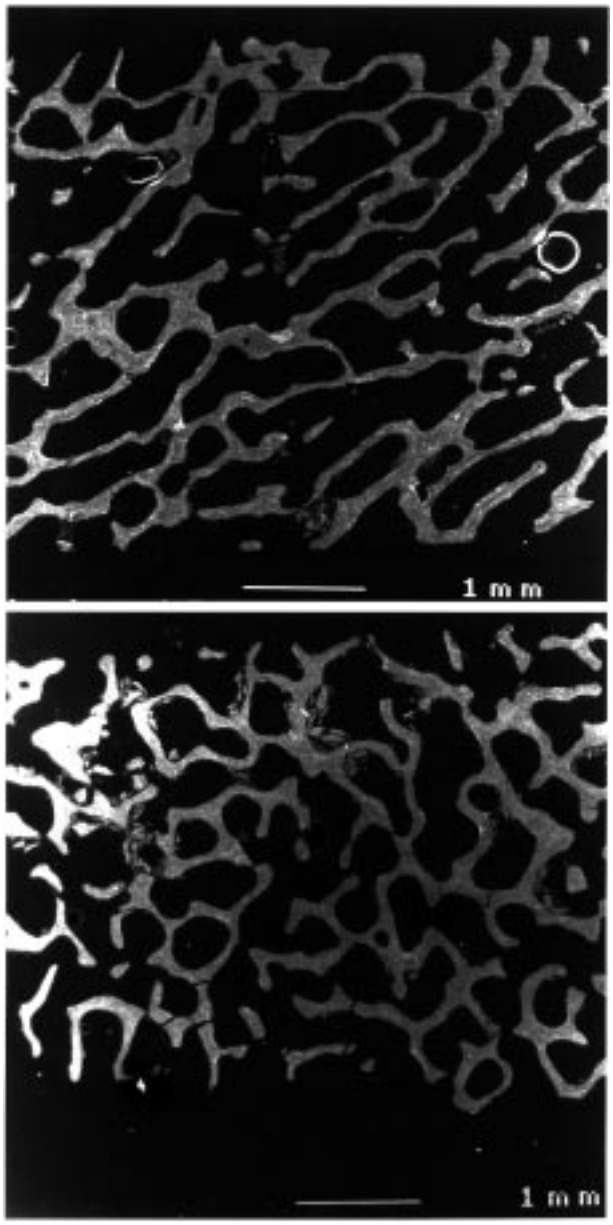

(b)

Figure 3 (b) Scanning electron micrographs demonstrating the effects of anisotropy on the macrostructure of specimens with similar densities.

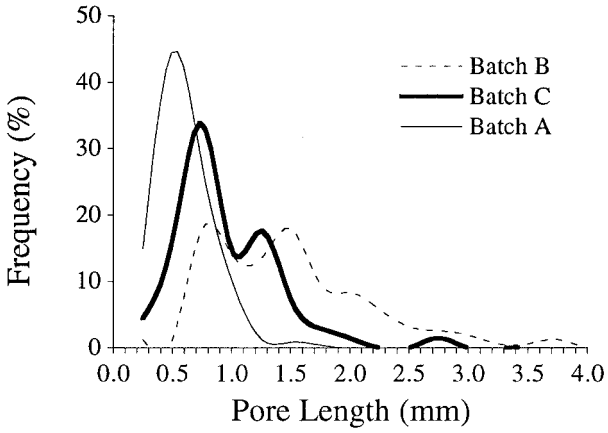

(a)

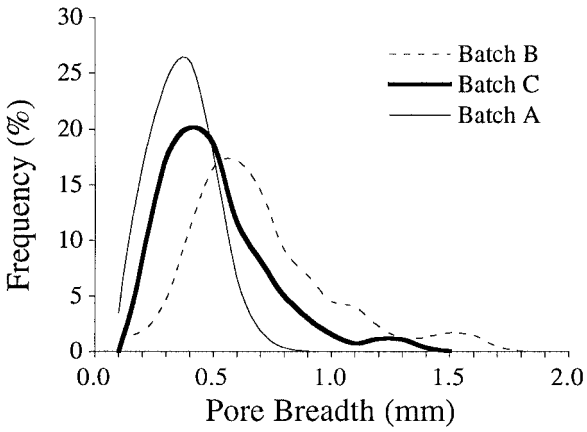

(b)

Figure 4 Variations in macropore (a) length and (b) breadth.

ally positioned within grains (Fig. 7a). Micropores $>3\,\mu m$ in size appeared to be interconnected, ellipsoidal in shape (approximately $10\,\mu m$ long and $5\,\mu m$ wide) and oriented, with respect to their neighbors, within the ceramic struts (Fig. 7b). Image analysis of the relative proportions of the two the types of micropores within a polished, sectioned strut are detailed in Table III, while the frequency distribution of the micropore size is illustrated in Fig. 8. Although the $<3\,\mu m$ pores were more numerous, the $>3\,\mu m$ pores provided a greater contribution to the volume fraction of porosity. Endobon® specimens were found to possess a highly crystalline, equiaxed grain structure with a mean grain size (G_d) of $1.57 \pm 0.78\,\mu m$, with a modal value of $1.35\,\mu m$ (Fig. 7a).

3.3. Mechanical testing

All specimens were found to fail in a manner typical of an elastic—brittle foam, exhibiting a linear elastic region followed by a collapse-plateau dominated by brittle fracture of the struts. However, the specific mechanical properties of individual specimens were highly dependent on the apparent density with the ultimate compressive stress (UCS) increasing from approximately 1 to 11 MPa, while compressive modulus (E_c) increased from approximately 0.2 to 3.1 GPa, as the apparent

TABLE II Morphological data for macropores

Batch	Mean length	Modal length	Mean breadth	Modal breadth	Mean ECD	Modal ECD	Modal aspect ratio
B	1360 [680]	1500	640 [290]	550	820 [310]	700	2.3
C	790 [420]	750	450 [220]	400	510 [210]	500	1.8
A	390 [480]	500	310 [120]	350	350 [150]	400	1.5

All sizes in μm, standard deviations in square parentheses.

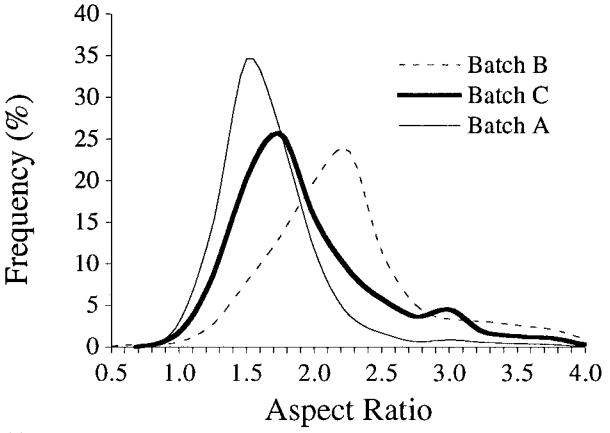

(a)

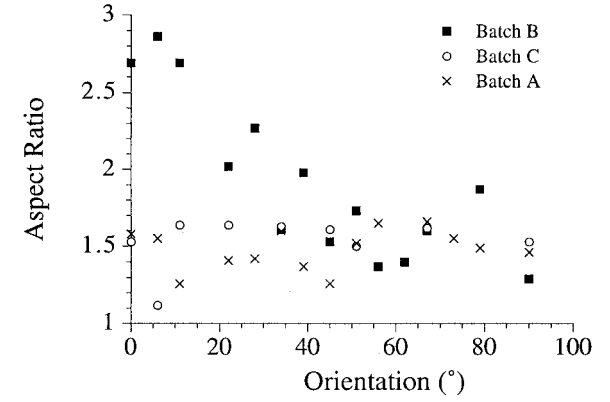

(b)

Figure 5 (a) Frequency distribution of macropore aspect ratios and (b) the relationship between pore shape and orientation for the three density batches.

density increased from 0.35 to 1.25 g cm^{-3}. Fig. 9a demonstrates that the relationship between the apparent density and UCS of isotropic specimens, in the range of densities tested, could be best described by a quadratic relationship. Anisotropy was not found to have a significant effect on the absolute values of UCS for specimens of comparative density, within the apparent density range tested (Fig. 9b). However, the UCS values of the anisotropic specimens were linearly related to the apparent density.

The E_c was also found to be strongly related to the apparent density and as with the UCS data, the segregated E_c data for both isotropic and anisotropic specimens were found to fit quadratic and linear

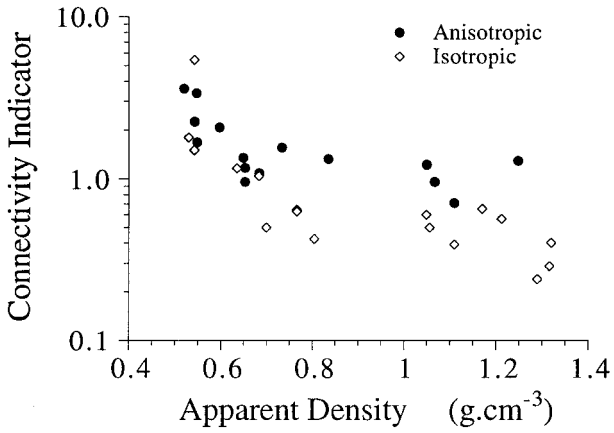

Figure 6 Variation in connectivity with apparent density.

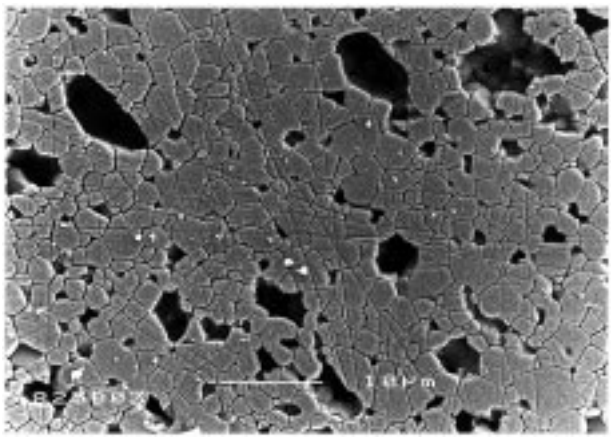

(a)

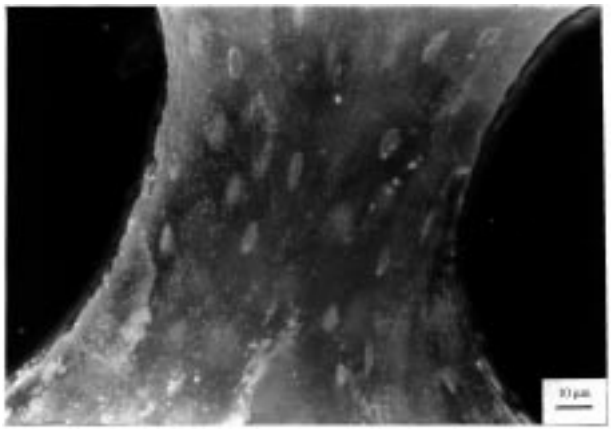

(b)

Figure 7 (a) Detail of the microstructure of an Endobon® strut in cross-section. (b) Darkfield illumination of polished thick sections of Endobon®, demonstrating the alignment of large micropores within the ceramic struts.

relationships respectively (Fig. 10). However, unlike the UCS, the effect of anisotropy on absolute values of E_c was more distinct, with a trend towards a reduced value of E_c for anisotropic specimens at higher apparent densities (Fig. 10b).

4. Discussion

Hydroxyapatite and bone mineral are known to accommodate a considerable range of lattice substitutions [22, 23], therefore, due to the biological origin of the precursor material, it was expected that Endobon® would contain additional ionic species. The levels of sodium and magnesium present compared well to those found in bone mineral [4, 23] and both species are known to substitute for calcium [22, 23]. However, the calcium to phosphorus ratios (Table I), calculated from the results

TABLE III Image analysis of micropores

Micropore group	Mean micropore size (μm)	Calculated microporosity (%)
All	1.4 [1.2]	17.93 [6.09]
<3 μm	1.2 [0.6]	5.73 [0.69]
>3 μm	6.8 [2.3]	12.20 [5.51]

All sizes in μm, standard deviations in square parentheses.

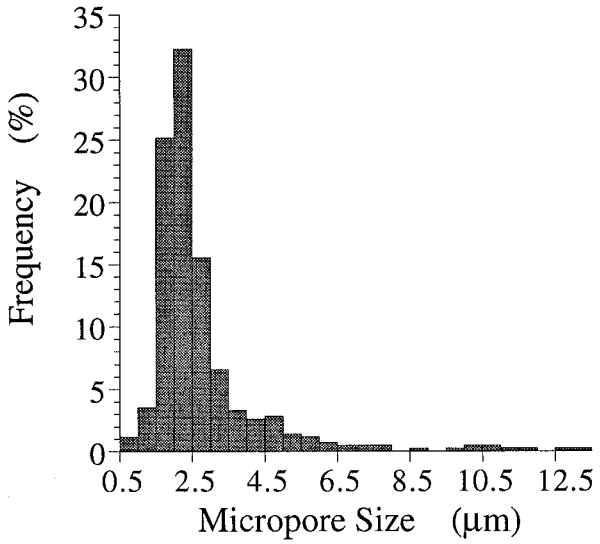

Figure 8 Frequency distribution of micropore size.

of the XRF analysis were greater than the theoretical value for stoichiometric hydroxyapatite of 1.67 indicating an increase in calcium content relative to phosphorus in the apatite lattice. This apparent anomaly was explained by the presence of a small peak at 37.4° in the XRD pattern which indicated that there was approximately 1–2 wt % of CaO present, which was likely to contribute to the elevated Ca:P ratio. Furthermore, the range of peaks at 1400–1550 in the FT-IR spectra for Endobon® indicated that the apatite was both A (OH^-) and B (PO_4^{3-}) type carbonate substituted (Fig. 2), thus the elevated Ca:P ratio will also reflect non-stoichiometric levels of PO_4^{3-} ionic groups as a result of B type CO_3^{2-} substitution. Bone mineral is believed to be primarily a B-type carbonate substituted apatite [23]; however, loss of CO_3^{2-} is likely to have occurred during the sintering and decarburization stage of Endobon® production [26], as is loss of OH^- [27]. Double substitution has been previously reported by Vignoles [25] and Barralet [24] in systems with far greater levels of carbonate substitution. Vignoles proposed that B type substitution only occurred after all the A sites were filled with carbonate (requiring approx. 4 wt % carbonate) while Barralet proposed that A and B sites were filled in equal proportions until half the A sites were filled, from this point he suggested that only B type substitution occurred. Because B type substitution has been observed in Endobon® powders with minimal carbonate contents (< 0.1 wt %) Barralet's mechanism seems the most suitable for description of the current data.

All specimens exhibited similar basic structural characteristics to a continuous open foam, with a three dimensional interpenetrating network of struts and pores. Some specimens also exhibited varying degrees of anisotropy, exhibited as an alignment of the long axis of high aspect ratio pores with the long axis of the cylindrical specimen. This structural variation was reflected by changes in the macropore size, shape, orientation and connectivity. As expected the modal values of macropore size decreased with increasing apparent density (Table II); however, it was also evident

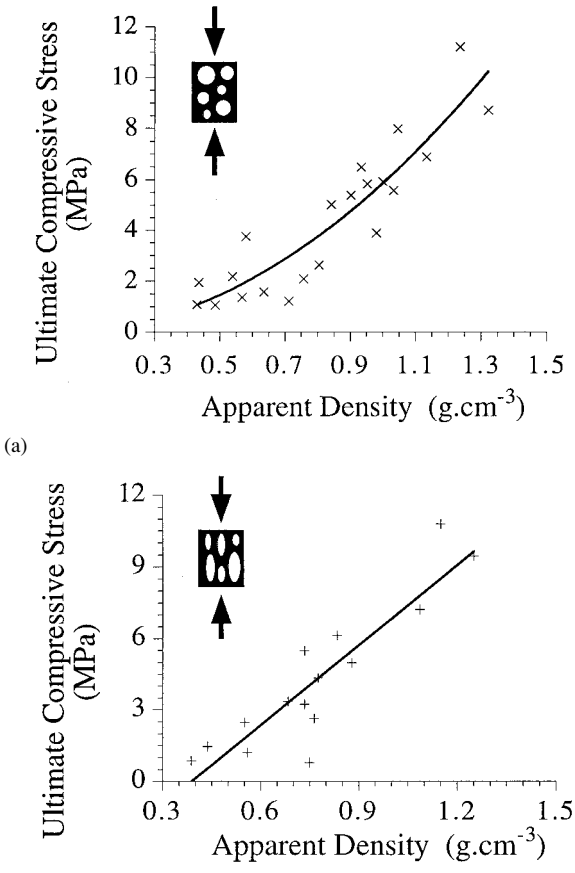

Figure 9 Effect of variation of the apparent density on the ultimate compressive strength of (a) isotropic and (b) anisotropic specimens.

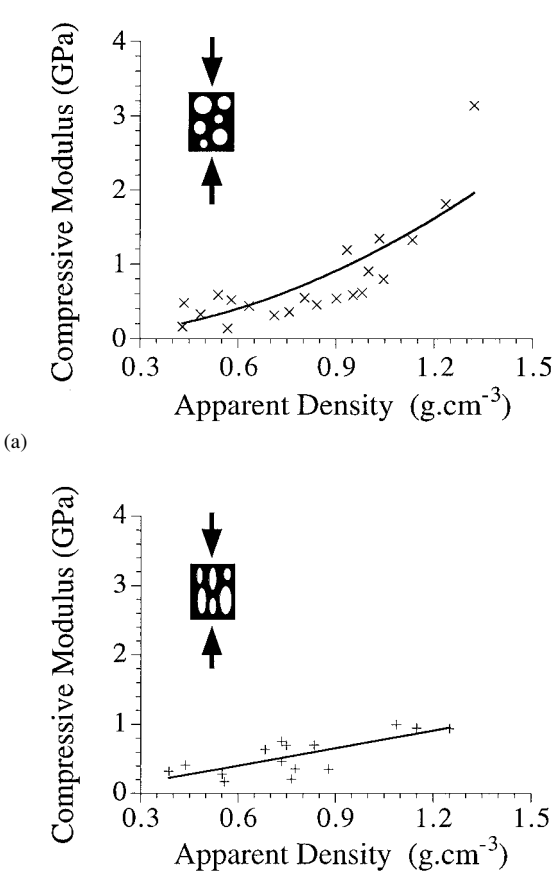

Figure 10 Effect of variation of the apparent density on the compressive modulus of (a) isotropic and (b) anisotropic specimens.

that the lower density Batch B specimens possessed broader macropore size ranges and aspect ratios than the other batches. These results reflected two populations of pores within Batch B, i.e. those within an anisotropic structure and those within an isotropic structure, which is consistent with the bimodal nature of the distribution of Batch B pore lengths (Fig. 4a). The distribution of pore breadths was monomodal for all specimens with less variation in the modal value from high to low density specimens, indicating the maintenance of a minimum modal pore size in the transverse direction for all structures, either isotropic or anisotropic (Fig. 4b).

Anisotropy was found to be characterized by a change in pore shape from round to elliptical with an alignment of the long axis of the pore to the long axis of the cylindrical specimen. The correlation between macropore aspect ratio and orientation in the low density specimens demonstrated a predominance of anisotropy in these specimens and highlighted the fact that specimens with greater anisotropy possessed pores with higher aspect ratios and more uniform alignment. The alignment with the long axis of the cylinders agreed well with the fact that the long axis of the cylinders was in turn parallel to the long axis of the bone of origin (either the femur or humerus). When considering Wolff's law [39], which states that bone will remodel to meet its physical requirements with the minimum safe weight, it is not surprising that the low density material tended to be anisotropic, as uniaxial loading will result in the production of lower density structures than isotropic loading to the same magnitude. This phenomenon was demonstrated in a study of trabecular structure in the human femoral head [40]. The authors found that open anisotropic structures predominated in low stress regions, while denser isotropic structures developed where stresses were elevated.

The connectivity of a porous implant is believed to play an important role in encouraging tissue ingrowth [10–12]. In Endobon® specimens, both the apparent density and the anisotropy appeared to effect this parameter. Where specimens were isotropic, connectivity was highly dependent on apparent density, however, for anisotropic specimens the influence of apparent density on connectivity was reduced. This reduction was due to an increase in apparent density of anisotropic specimens, manifesting as an increase in strut thickness rather than in strut number (and hence, pore and thus connection number).

The microstructure of Endobon® was not found to vary with apparent density. Specimens were found to have a real density of $3.009 \pm 0.038\,\mathrm{g\,cm^{-3}}$, which equates to approximately 94–97% of the theoretical density of hydroxyapatite, i.e. containing 3–6% closed microporosity. However, inspection of cross-sections of Endobon® specimens indicated that the total microporosity within the struts was, on average, 18%. This discrepancy between the results of microscopic observation and density measurement, was found to result from the ability of the density measurement technique to assess only closed porosity. The $<3\,\mu\mathrm{m}$ micropores, which were formed during the sintering process as a result of grain growth and coalescence, were located on triple points and within grains and as such would be expected to be isolated from both each other and the external surfaces. Conversely, the size and alignment of the larger elliptical pores suggest that these pores may be preserved osteocyte lacunae from the original microstructure of the bone [41] and as such would be interconnected with one another and the macropores. Hence, the result from the density measurement would include only the contribution of the $<3\,\mu\mathrm{m}$ micropores.

Endobon® was found to possess a highly crystalline structure, the grains were generally equiaxed in shape with a modal grain size of $1.35\,\mu\mathrm{m}$. This represents a significant change from the starting material, which would have been composed predominantly of unsintered bone mineral, with a plate or rod like morphology and dimensions in the region of approximately 2–50 nm [22, 23]. This change in size and morphology can be explained by considering the high interfacial energy possessed by a ceramic with nanometer sized acicular grains. By increasing the grain size and changing the grain morphology to a more equiaxed shape, the internal surface to volume ratio would be reduced, so decreasing the surface energy of the individual crystallites and the ceramic body as a whole.

The mechanical properties of dense synthetic hydroxyapatite, as with all engineering ceramics, are highly dependent on the processing route, as a consequence of the effects of processing on the microstructure of the final product. This dependency results from mechanical sensitivity to parameters, such as variations in grain size, micropore size and micropore distribution. However, for the highly porous (<50% dense) Endobon® specimens the macroporosity appears to be the dominating factor in determining the mechanical properties, particularly as the microstructure was uniform for all specimens. Both ultimate compressive stress and modulus increased by a factor of approximately 10 over the apparent density range tested (0.38 to $1.25\,\mathrm{g\,cm^{-3}}$) which represents a change from 10 to 40% dense. These results demonstrate the extreme sensitivity of the mechanical properties of porous ceramics to porosity, at these low densities. Moreover, there were highly correlated relationships between the mechanical properties and the apparent densities of the Endobon® specimens.

In this investigation, the application of a quadratic relationship between UCS and E_c, as proposed for isotropic, open, elastic–brittle, ceramic foams [34, 35] was found to be highly successful. Furthermore, the data for anisotropic specimens was found to be described by linear relationships, as predicted. Regression analysis of the data indicated a strong correlation between the experimental results and the theoretical relationships (Table IV). The variation in behavior with structure highlighted the sensitivity of E_c to isotropy in higher density specimens (Fig. 10). For example, the E_c of a specimen with an apparent density of $1.5\,\mathrm{g\,cm^{-3}}$ is predicted to vary from 1.2 to 2.5 GPa as a result of changes in isotropy. The increased sensitivity of E_c to anisotropy may be a result of changes in the failure mechanisms of higher density anisotropic foams as a result of strut wall thickening. Increases in the longitudinal strut wall thickness will result in failure by brittle fracture initiated at defect sites on the strut surfaces and

TABLE IV Relationships between mechanical properties and apparent density

Data	Equation	r	Equation No
All UCS data	$UCS = 6.15\,\rho^2$	0.90	(8)
Isotropic UCS data:	$UCS = 5.86\,\rho^2$	0.91	(9)
Anisotropic UCS data: UCS = 11.20 ρ − 4.34	0.90	(10)	
Isotropic E_c data:	$E_c = 1.12\,\rho^2$	0.84	(11)
Anisotropic E_c data:	$E_c = 0.85\,\rho - 0.10$	0.75	(12)

at junctions with cross struts, as opposed to buckling and fracture, which is assumed to be the principle failure mode in lower density anisotropic specimens. Furthermore, the study of specimen cross-sections demonstrated that the cell walls in high density, anisotropic specimens were consistently thicker than comparative isotropic specimens of similar density.

5. Conclusions

The combined results of the chemical analysis demonstrate the complicated chemistry of apatites, and hence, the need for a full analytical study of these ceramics for adequate characterization. In this work the chemical analysis demonstrated that the natural apatite precursor was not converted to pure hydroxyapatite, but retained some of the ionic substituents found in bone mineral, notably carbonate, magnesium and sodium.

Macrostructure was found to vary considerably, as a function of both apparent density and structural architecture. This variation was reflected by increases in the modal pore size and pore connectivity with a decrease in apparent density. Pore shape (aspect ratio) and pore orientation were found to reflect the degree of anisotropy of a structure, where low density specimens tended to exhibit a greater degree of anisotropy, with elongated pores (or struts) having a preferred orientation parallel to the long axis of the cylindrical specimens. This anisotropy was found to affect the degree of connectivity in high density structures.

Microstructural analysis demonstrated that the microporosity did not vary significantly with apparent density, and that specimens possessed a uniform, equiaxed grain structure. The modal grain size was found to be considerably greater than the reported size of bone mineral crystals. However, other aspects of the trabecular microstructure, such as the network of osteocyte lacunae, were found to be partly preserved and the presence of these features led to a relatively high degree of ''strut porosity''.

Mechanical testing indicated that as-received Endobon® behaved as an elastic brittle foam when loaded under conditions of uniaxial compression. The ultimate compressive stress and E_c increased from 1 to 11 MPa and 0.2 to 3.1 GPa, respectively, as apparent density increased from 0.38 to 1.25 $g\,cm^{-3}$. These results demonstrate the extreme sensitivity of the mechanical properties of porous ceramics to apparent density at these low densities.

Furthermore, anisotropic high density (> 0.9 $g\,cm^{-3}$) specimens were found to possess lower compressive moduli than equivalent isotropic specimens. Thus a simple density measurement should be combined with an assessment of isotropy to accurately screen for mechanical integrity.

Acknowledgment

The authors gratefully acknowledge the Engineering and Physical Sciences Research Council (UK) for the core grant funding of the IRC in Biomedical Materials and the support of E. Merck GmbH (Germany).

References

1. M. JARCHO, C. H. BOLEN, M. B. THOMAS, J. BOBICK, J. F. KAY and R. H. DOREMUS, *J. Mater. Sci.* **11** (1976) 2027.
2. H. W. DENISSEN, K. DE GROOT, A. A. DRIESSEN, J. G. C. WOLKE, J. G. J. PEELEN, H. J. A. VAN DIJK, A. P. GEHRING and P. J. KLOPPER, *Sci. Ceram.* **10** (1980) 63.
3. G. DE WITH, H. J. A. VAN DIJK, N. HATTU and K. PRIJS, *J. Mater. Sci.* **16** (1981) 1592.
4. H. AOKI, ''Science and medical applications of hydroxyapatite'' (Takayama Press, Tokyo, 1991).
5. ''Osseo-integrated implants'' edited by G. Heimke (CRC Press, Boca Raton, 1990) p. 2.
6. P. K. STEPHENSON, M. A. R. FREEMAN, P. A. REVELL, J. GERMAN, M. TUKE and C. J. PIRIE, *J. Arthroplasty* **6** (1991) 51.
7. A. MORONI, V. J. CAJA, E. L. EGGER, L. TRINCHESE and E. Y. S. CHAO, *Biomaterials* **15** (1994) 926.
8. J. D. DE BRUIJN, PhD thesis, University of Leiden, 1993.
9. S. BEST, B. SIM, M. KAYSER and S. DOWNES, *J. Mater. Sci.: Mater. Med.* **8** (1997) 97.
10. J. H. KÜHNE, R. BARTL, B. FRISH, C. HANMER, V. JANSSON and M. ZIMMER, *Acta Orthop. Scand.* **65** (1994) 246.
11. P. S. EGGLI, W. MULLER and R. K. SCHENK, *Clin. Orthop. Rel. Res.* **232** (1988) 127.
12. R. E. HOLMES, V. MOONEY, R. BUCHOLZ and A. TENCER, *ibid.* **188** (1984) 252.
13. S. H. MAXIAN, J. P. ZAWADDSKY and M. G. DUNN, *J. Biomed. Mater. Res.* **27** (1993) 717.
14. L. SMITH, *Arch. Surg.* **87** (1963) 653.
15. S. F. HULBERT, J. S. MORRISON and J. J. KLAWITTER, *J. Biomed. Mater. Res.* **6** (1972) 347.
16. J. J. KLAWITTER and S. F. HULBERT, *ibid.* **5** (1971) 161.
17. N. J. GARRAHAN, R. W. E. MELLISH and J. E. COMPSON, *J. Microsc.* **142** (1986) 341.
18. E. C. SHORS, E. W. WHITE and R. M. EDWARDS, in ''Quantitative characteristics and performance of porous implants for hard tissue applications'', edited by J. E. Lemons (ASTM STP 953, 1987) p. 347.
19. R. HODGSKINSON and J. D. CURREY, *Proc. Inst. Mech. Engrs.* **204** (1990) 115.
20. K. H. LAU, A. YOO and S. PING-WANG, *Mol. Cell Biochem.* **105** (1991) 93.
21. P. LI, C. OHTSUKI, T. KOKUBO, K. NAKANISHI, N. SOGA and K. DE GROOT, *J. Biomed. Mater. Res.* **28** (1994) 7.
22. A. S. POSNER, *Physiol. Rev.* **49** (1969) 760.
23. R. Z. LE GEROS and J. P. LE GEROS, in ''An introduction to bioeramics'' edited by L. L. Hench and J. Wilson (World Scientific, Singapore, 1993).
24. J. BARRALET, PhD Thesis, University of London, 1995.
25. C. VIGNOLES, University of Toulouse, France, 1984.

26. I. ABRAHAMS and J. C. KNOWLES, *J. Mater. Chem.* **4** (1994) 185.
27. P. E. WANG and T. K. CHAKI, *J. Mater. Sci.: Mater. Med.* **4** (1993) 150.
28. N. C. BLUMENTHAL and A. S. POSNER, *Calc. Tiss. Int.* **36** (1984) 439.
29. N. C. BLUMENTHAL and M. S. COSMA, in ''Tissue-inducing biomaterials'' edited by L. Cima and E. Ron, *Mat. Res. Soc. Symp. Proc.* **252** (1992) 29.
30. W. J. A. DHERT, C. P. A. T. KLEIN, J. G. C. WOLKE, E. A. VAN DER VELDE, K. DE GROOT and P. M. ROZING, *J. Biomed. Mater. Res.* **25** (1991) 1183.
31. J. D. CURREY, *Clin. Orthop. Rel. Res.* **73** (1970) 210.
32. F. LINDE, I. HVID and F. MADSEN, *J. Biomechanics* **25** (1992) 359.
33. T. M. KEAVENY, R. E. BORCHERS, L. J. GIBSON and W. C. HAYES, *ibid.* **26** (1993) 991.
34. L. J. GIBSON, *J. Biomech.* **18** (1985) 317.
35. L. J. GIBSON and M. F. ASHBY, in ''Cellular solids'' (Pergamon Press, Oxford, 1988).
36. K. A. HING, S. M. BEST, P. A. REVELL, K. E. TANNER and W. BONFIELD, *J. Mater. Sci.: Mater. Med.* **8** (1997) 731.
37. Powder Diffraction File (PDF) 9-432, International Committee for Diffraction Data (ICDD), Newton Square, Pennsylvania, USA.
38. Powder Diffraction File (PDF) 37-1497, International Committee for Diffraction Data (ICDD), Newton Square, Pennsylvania, USA.
39. J. WOLFF, *Virchows Arch. Path. Anat. Physiol.* **50** (1870).
40. W. J. WHITEHOUSE and E. D. DYSON, *J. Anat.* **118** (1974) 417.
41. P. A. REVELL, in ''Pathology of bone'' (Springer-Verlag, Berlin, 1986).

Received 12 June
and accepted 13 July 1998